STARS

University of Central Florida
STARS

Honors Undergraduate Theses

UCF Theses and Dissertations

2021

Analysis of Bending Waves in Saturn's Rings

Claudia Denise Orozco Vega
University of Central Florida

 Part of the The Sun and the Solar System Commons
Find similar works at: https://stars.library.ucf.edu/honorstheses
University of Central Florida Libraries http://library.ucf.edu

This Open Access is brought to you for free and open access by the UCF Theses and Dissertations at STARS. It has been accepted for inclusion in Honors Undergraduate Theses by an authorized administrator of STARS. For more information, please contact STARS@ucf.edu.

Recommended Citation

Orozco Vega, Claudia Denise, "Analysis of Bending Waves in Saturn's Rings" (2021). *Honors Undergraduate Theses*. 1002.
https://stars.library.ucf.edu/honorstheses/1002

University of Central Florida
STARS
Showcase of Text, Archives, Research & Scholarship

ANALYSIS OF BENDING WAVES IN SATURN'S RINGS

by

CLAUDIA OROZCO VEGA

A thesis submitted in partial fulfillment of the requirements
for the Honors in the Major Program in Physics
in the College of Sciences
and in the Burnett Honors College
at the University of Central Florida
Orlando, Florida

Spring Term, 2021

Thesis Chair: Dr. Joshua Colwell

ABSTRACT

Saturn's rings are a complex, dynamic system that can provide unique insight into the structure and features of the planet and surrounding system. We use stellar occultation data of Saturn's rings collected from the Cassini Ultraviolet Imaging Spectrograph to visualize and analyze bending waves present within the rings. Analysis of the propagation of these waves gives insight into the surface mass density of the local ring region and can be used to further our understanding of ring dynamics and ring formation. Our analysis of the Mimas 7:4 bending wave estimated a surface mass density between 30 g cm^{-2} and 43 g cm^{-2}, corroborating the findings of Spilker *et al.* (2004) of 47 ± 6.2 g cm^{-2} and supporting our current understanding of linear wave theory. Our analysis of the Mimas 4:2 bending wave estimated the surface mass density to be between 33 g cm^{-2} and 47 g cm^{-2} and was of particular interest since this wave is found in the relatively uncharacterized B ring region.

TABLE OF CONTENTS

ABSTRACT 2

LIST OF FIGURES 4

LIST OF TABLES 6

1. INTRODUCTION 7

2. THE VOYAGER AND CASSINI MISSIONS 11

3. OBSERVATIONS 16

4. METHODS 24

4. RESULTS AND CONCLUSIONS 28

LIST OF FIGURES

Figure 1. Image of Saturn's rings taken from the Cassini spacecraft. Image: NASA/JPL/Space Science Institute 8

Figure 2. Diagram of spiral density wave structure in Saturn's rings showing regions of high and low particle density in nested rotated elliptical orbits with Saturn in the center. 9

Figure 3. Image taken by the Cassini spacecraft showing a density wave (left) and a bending wave (right) in Saturn's A ring. Image: NASA/JPL-Cassini/SSI. 10

Figure 4. Illustration of a stellar occultation. Figure not to scale. 15

Figure 5. Occultation data of the rings from BetCen 077I, binned by 1000 (see Colwell et al., 2010 for explanation of binning). 17

Figure 6. Illustration of Cassini stellar occultation incidence angle, B, of a bending wave (solid black line) compared to the horizontal ring plane. The vertical scale is greatly exaggerated. The dashed lines represent the line-of-sight between Cassini and the star at different points on the wave. Peaks in optical depth are marked by red asterisks, while troughs are marked with blue asterisks. 17

Figure 7. Optical depth profile of the rings from BetCen 077I. 19

Figure 8. The top image shows the relative position of Saturn's rings and moons, and the bottom plot by Colwell et al. (2009) shows the optical depth profile of the C, B, and A rings as well as that of the Cassini division. 20

Figure 9. Raw data from BetCen 077I in the Mimas 5:3 DW region. Resonance location is marked in red. 22

Figure 10. Optical depth profile of the Mimas 5:3 DW from BetCen 077I with resonance location marked in red. 22

Figure 11. Optical depth profile of the Mimas 5:3 bending wave from AlpVir 116I, with the resonance location marked in red. 23
Figure 12. Weighted wavelet transform of the Mimas 5:3 BW from α Vir (dashed red line). The resonance location for the Mimas 5:3 BW is marked in red. The Prometheus 12:11 DW (dashed blue line) is also visible, propagating in the opposite direction. 23
Figure 13. A Morlet wavelet 25
Figure 14. Weighted wavelet transform of the region surrounding the Mimas 7:4 BW using data from a single KapOri occultation. The resonance location of the Mimas 7:4 BW is marked in red. 27
Figure 15. Wavelet transform of the Mimas 7:4 BW (red dashed line) using combined data from 4 KapOri occultations. The resonance location is marked in red. The Prometheus 8:7 DW is also distinctly visible on top of the Mimas 7:4 BW (blue dashed line) 27
Figure 16. Wavelet profile of the Mimas 7:4 BW (red dashed line) from combined AlpVir and KapOri occultations, resonance location marked in red. The Prometheus 8:7 DW is also distinctly visible on top of the Mimas 7:4 BW (blue dashed line). 29
Figure 17. Wavelet profile of the Mimas 4:2 BW from 17 combined AlpVir occultations. 29

LIST OF TABLES

Table 1 Surface mass density calculations by Lissauer (1985) 12

Table 2 List of occultations..... 18

1. INTRODUCTION

Saturn's rings are a complex, dynamic system made up of small particles, mainly of crystalline water, which constantly interact with each other via self-gravity and aggregate, forming larger clumps before eventually breaking apart again (Esposito, 2009). The size of the particles is variable within and between the rings, with Esposito (2009) estimating a size range of 1-30 cm for the smallest ring particles and 2-20 m for the largest particles and clumps. The larger ring structure is marked by features ranging from small, embedded moons to propagating waves of particles extending hundreds of kilometers (Esposito, 2009). Embedded moons within the ring plane, forces from Saturn's interior, as well as collisions and self-gravity between the ring particles all interact to create the variety of structures observable in the rings, ranging from gaps hundreds of kilometers wide to wakes and waves stretching across the rings. Figure 1 shows several of these features, including bright spots known as "spokes" that are thought to be caused by electromagnetic phenomena and impact to the rings (Cuzzi *et al.*, 2002). Studying and modeling these features helps us to understand the physical processes underlying their creation, and thus further our understanding of larger cosmic systems that share a similar structure (i.e., spiral galaxies) (Esposito, 2009). A more in-depth description of the rings is available in Colwell *et. al* (2009).

One of the most common features seen in the rings are density waves, which are caused when ring particles' orbital motions are resonantly perturbed by gravitational forces from one of Saturn's moons. This type of resonance is referred to as a Lindblad resonance, which occurs when the epicyclic frequency of an object (in this case, the ring particles at a specific orbital distance from Saturn) is equal to a whole-number multiple of the forcing frequency of another object (in this case, a moon). The epicyclic frequency is the frequency of the periodic radial

motion of a particle on an elliptical orbit. When this frequency is resonantly forced by gravitational perturbations from a moon, the eccentricity of the ring particles at the resonance location grows, leading to enhanced collisions with neighboring particles. These ring particles then interact with other ring particles nearby via gravity and collisions, causing waves of alternating increased and decreased particle packing density, similar to that of a sound wave. These waves propagate toward the perturbing moon. The overall structure of the waves is that of spiral arms similar to those observed in spiral galaxies (Fig. 2), but much more tightly wound due to the wavelength being much smaller than the orbit size. See Colwell *et al.* (2009) for an overview of density waves in Saturn's rings.

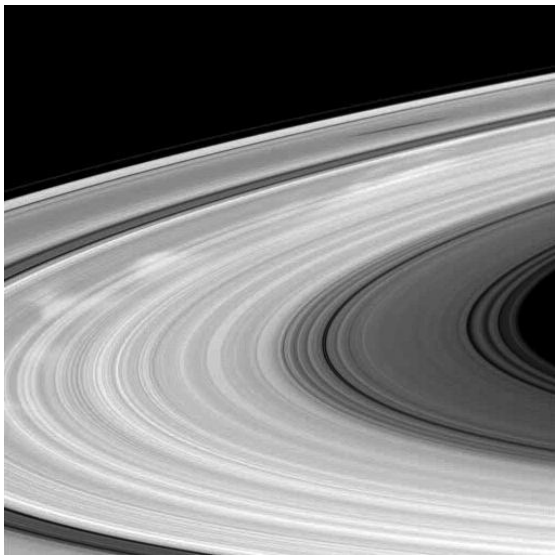

Figure 1. Image of Saturn's rings taken from the Cassini spacecraft. Image: NASA/JPL/Space Science Institute

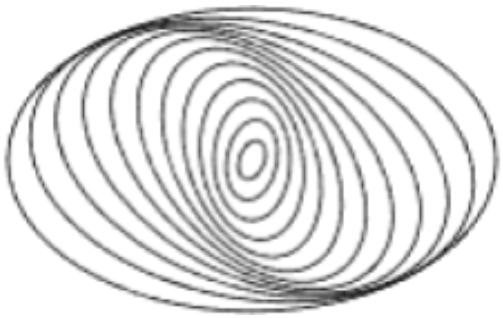

Figure 2. Diagram of spiral density wave structure in Saturn's rings showing regions of high and low particle density in nested rotated elliptical orbits with Saturn in the center.

The focus of this research is a type of less commonly occurring wave known as a bending wave. Bending waves are also caused by an orbital resonance with a nearby moon, but specifically in cases where the moon's orbit is inclined compared to Saturn's main ring plane (Gresh *et al.*, 1986). This exerts a perpendicular force relative to the ring plane, causing a vertical oscillation of the ring particles that propagates away from the moon, rather than toward it, as a spiral bending wave (Gresh *et al.*, 1986). In this case, the moon's motion is resonant not with the ring particle's epicyclic frequency but with its vertical frequency, the natural frequency of its out-of-plane motion as it orbits Saturn on an inclined orbit. Because of Saturn's oblateness, the locations of Lindblad resonances and vertical resonances are not at the same place. Figure 3 shows a bending wave and a density wave propagating in opposite directions. Alternating bands of light and dark show the wavelength, which gets shorter as the wave moves away from resonance. Bending waves are much less common than density waves due to the fact that first-order resonances, the strongest type, do not occur in vertical resonances. In addition, the inclinations of the moons causing these resonances relative to Saturn's ring plane are relatively small (Tiscareno et al., 2007). The moon Mimas, with an inclination of approximately 1.574º relative to the ring plane, is responsible for producing many of the stronger bending waves found

within the rings. The most prominent bending wave in the rings, the Mimas 5:3 BW, has been extensively characterized. The numbers denoting a resonance, such as 5:3, are approximately equal to the ratio of the ring particle's orbital frequency to the perturbing moon's orbital frequency (Colwell *et al.*, 2009). Tiscareno et al. (2018) used images from cameras on the Cassini spacecraft to characterize several previously unidentified waves and wave-like features in the rings that likely represent bending waves.

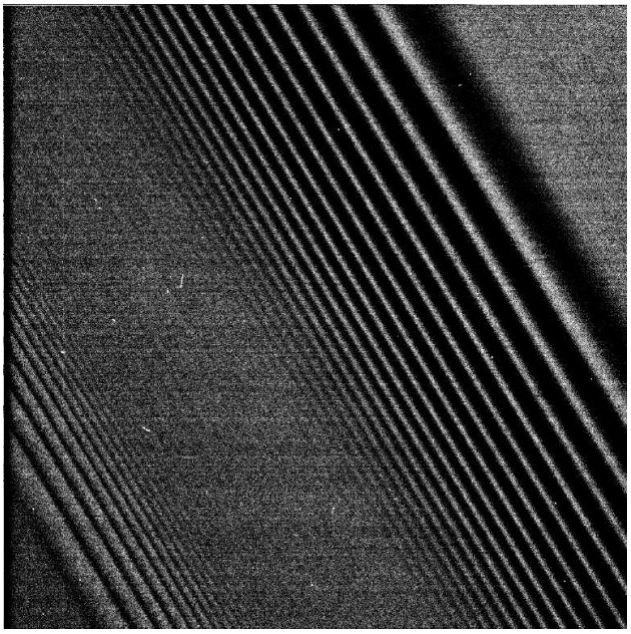

Figure 3. Image taken by the Cassini spacecraft showing a density wave (left) and a bending wave (right) in Saturn's A ring. Image: NASA/JPL-Cassini/SSI.

The next section contains an overview of previous analysis conducted on data collected from the Voyager and Cassini missions. Section 3 contains a description of the stellar occultation observations we analyzed while Section 4 describes the analysis techniques used. The final section presents and discusses the observations, local surface mass densities, and how these relate to our current understanding of wave theory.

2. THE VOYAGER AND CASSINI MISSIONS

Cuzzi *et al.* (2002) summarize the understanding of Saturn's ring structure and dynamics prior to the Cassini mission, focusing on the data collected from the Voyager missions. The Voyager 1 and 2 probes, which reached the Saturn system in 1980 and 1981 respectively, included a two-camera system with both a narrow- and wide-angle camera as well as several wavelength filters that allowed for the first high-resolution images of Saturn to be collected and studied (Cuzzi *et al.*, 1981). The Voyager probes also included a Radio Science System, which used radio signals of a specific wavelength to perform stellar occultations. A stellar occultation occurs when a star is visible behind a ring system and is partially blocked by the ring particles, causing changes in its measurable brightness as viewed from behind the rings (Fig. 4). The angle between the line-of-sight between where the star is observed and the ring plane is the incidence angle. The Voyager Photopolarimeter Subsystem (PPS) also conducted limited stellar occultations, producing approximately 39 counts every 10 ms for its occultation of δ Scorpio, but its observations were limited in regions where the rings were particularly dense. The first theory of forced bending waves in Saturn's rings was developed by Shu *et al.* (1983) via analysis of images of Saturn's rings from the Voyager mission. They observed that specific variations in apparent brightness of the rings were due to vertical folds of the local ring plane (bending waves), and that the likely cause of these was vertical resonance with the moon Mimas. Lissauer (1985) also used Voyager images to characterize the Mimas 4:2, 5:3, 7:4, and 8:5 bending waves and used this data to determine the surface mass density of various ring regions. Surface mass density (σ) refers to the total mass of particles per unit area, which depends on how tightly packed the ring particles are, the particle density, and the vertical thickness of the ring at that area. Through the relationship that exists between the wavelength of these waves and their radial

location relative to Saturn, it is possible to determine the local σ of the rings (see Chapter 3 below). Lissauer (1985) used this relationship to calculate the σ of the Mimas 5:3, Mimas 7:4, Mimas 4:2, and Mimas 8:5 regions (results summarized in Table 1). Spilker *et al.* (2004) also used Voyager data to identify and analyze 40 spiral density waves in the A ring, calculating the average σ of the inner three-quarters of the A ring to be 43.8 ± 7.9 g cm^{-2} and the outer one-fourth average σ to be 28.3 ± 10.8 g cm^{-2}. Gresh *et al.* (1986) used Voyager 1 radio occultation data to determine if the Mimas 5:3, 7:4, and 4:2 spiral bending waves adhered to the linear model for bending waves developed in Shu *et al.* (1983). Due to limitations in the signal-to-noise ratio of the data, Shu *et al.* (1983) were only able to draw their conclusions from analysis of the Mimas 5:3 bending wave and the Mimas 7:4 bending wave, both of which supported linear wave theory.

Table 1 Surface mass density calculations by Lissauer (1985)

Ring Region	Surface Mass Density (σ)
Mimas 5:3	45 ± 2 g cm^{-2}
Mimas 7:4	39 ± 4 g cm^{-2}
Mimas 4:2	54 ± 10 g cm^{-2}
Mimas 8:5	24 ± 3 g cm^{-2}

Cuzzi *et al.* (2002), in addition to summarizing Voyager data, described the objectives of the Cassini mission and the various instruments on the spacecraft, which represented marked improvements from those aboard the Voyager missions. Similar to the Voyager probes, the Cassini spacecraft included both a Radio Science Subsystem (RSS) and a dual-camera Imaging Science Subsystem (ISS). The RSS used multiple wavelength occultations to map structures

within the rings (Cuzzi *et al.*, 2002). The Cassini RSS improves on the Voyager RSS due to its ability to analyze data over three wavelengths, as well as its increased opportunities to perform occultations of the same regions (Cuzzi *et al.*, 2002). The ISS Narrow Angle Camera (NAC), with a typical resolution of 6 microradians, and the ISS Wide Angle Camera (WAC), with a typical resolution of 60 microradians (Cuzzi *et al.,* 2002) both represented a much higher resolution than the Voyager cameras and allowed for observation and analysis of many more ring features. The ISS is explained in more detail in Porco *et al.* (2004) and in Cuzzi *et. Al* (2002). Porco *et al.* (2007) also contains images obtained by the ISS as well as how to calibrate, process, and present this data. The data in this research was collected by the Cassini Ultraviolet Imaging Spectrograph (UVIS), which used UV radiation to provide the highest spatial resolution of any of the instruments. The high absorption of UV radiation by the rings significantly reduces background signal, and their small wavelength makes them sensitive to even very small ring particles (Cuzzi *et al.,* 2002). Both Esposito *et al.* (1998) and Esposito *et al.* (2004) go into greater detail about the specifications of the Cassini Ultraviolet Imaging Spectrograph (UVIS), as well as how the data it collected can provide valuable insight into the dynamics of the rings, characteristics of the ring particles at different locations, and data useful for the creation of mathematical models of the rings. Finally, the Visual and Infrared Mapping Spectrometer (VIMS) aboard Cassini provided information about the material within the rings and was also able to conduct stellar occultations using infrared (IR) radiation. This allowed it to observe a different classification of stars than those observable by UVIS (Cuzzi *et al.,* 2002).

The stellar occultation data collected from UVIS represents a marked improvement from that of the Voyager mission. With a resolution close to 20 m, UVIS is able to probe structures approximately five times narrower than Voyager and with 50 times the sensitivity (Esposito *et*

al., 1998) (Cuzzi *et al.*, 2002). In addition, UVIS produced approximately 2000 counts per 2 ms in its occultations compared to the Voyager PPS's 39 counts per 10 ms (Esposito *et al.*, 1998). Baillie *et al.* (2011) used UVIS data and co-added wavelet transforms to analyze 62 stellar occultations in the C ring, characterizing several inwardly propagating waves only visible at small-incidence-angle occultations as possible bending waves and using data from these to determine various features of the C ring, including its vertical thickness and its estimated mass. Bending waves are more suitable for this purpose when compared to density waves in regions of high optical depth and high structural irregularity where density waves are obscured (Lissauer, 1985). In addition, by analyzing stellar occultation data from VIMS, Hedman and Nicholson (2013) found evidence of density waves in the C ring that were caused by cyclic gravitational oscillations from within Saturn itself as opposed to from a perturbing moon. Follow-up work by Hedman and Nicholson (2014) found more of these waves, analysis of which could give investigators new insights into Saturn's interior. Rappaport *et al.* (2020) used data from Cassini's Radio Science Subsystem (RSS) occultation observations to create a two-dimensional model of the Mimas 5:3 density wave, relying only on its four-armed structure and its predicted pattern speed. They also measured wavenumber across the Mimas 5:3 BW and used this to calculate a σ for the region, which varied by a factor of two (35 g $cm^{-2}$to 70 g cm^{-2}) within the wave. This is a departure from other studies that have determined a single σ for a ring region using the entire wave.

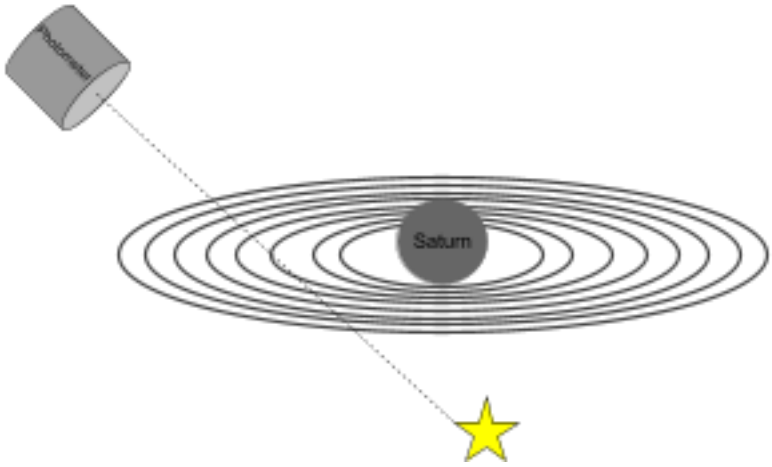

Figure 4. Illustration of a stellar occultation. Figure not to scale.

Colwell *et al.* (2009) utilized a weighted wavelet Z (WWZ) transform to analyze density waves in the Cassini Division and Cassini Division ramp (Fig. 8). Using this data along with that from previous studies to compare the ring particles in the Cassini Division with those of the Cassini Division ramp and the A ring, Colwell *et al.* (2009) concluded that the largest ring particles in the Cassini Division ramp and the A ring were about 5 times larger than the largest particles in the main Cassini Division. Hedman and Nicholson (2016) also conducted a wavelet-based analysis of several density waves in the B ring, overcoming the obstacle posed by the region's particularly high optical depth by combining data from several occultations to amplify the signals of weaker waves.

3. OBSERVATIONS

The Cassini space probe includes, among various other instruments, an Ultraviolet Imaging Spectrograph (UVIS) High Speed Photometer (HSP). The HSP counted UV photons from bright stars visible through Saturn's rings, taking measurements every 1-8 milliseconds (Colwell *et al.*, 2010). When a star was blocked by the rings, the photon count data would be measured and was referred to as a single occultation of that star (Fig. 5). Over the 13 years of the Cassini mission, some stars were observed multiple times by the HSP. In addition, an occultation may have distinct ingress and egress portions, resulting in measurement of the same ring plane radius twice at slightly different times and at different azimuths around the rings. Esposito *et al.* (2004) describes the specifications and configuration of the HSP, noting design features incorporated into its design in order to minimize signal variation and prevent sunlight reflecting off the rings to interfere with the stellar occultation data. Colwell *et al.* (2010) described a standard procedure for producing optical depth profiles from this data, which was followed when conducting this research. As Cassini is constantly in motion, the point where its line-of-sight to the star crosses the rings traces a linear path through the rings. The angle between this line-of-sight and the ring plane is called the incidence angle, *B*. Bending waves are only visible in occultations with a small incidence angle (Fig. 6). Our research used stellar occultation data collected from the Cassini space probe (Table 2) to identify and analyze bending waves, selecting occultations that spanned the appropriate ring region with low B angles and high signal-to-noise ratios.

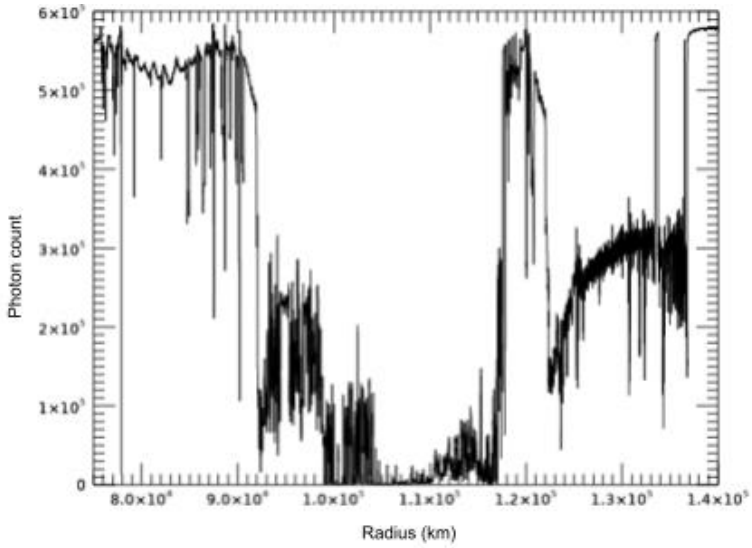

Figure 5. Occultation data of the rings from BetCen 077I, binned by 1000 (see Colwell et al., 2010 for explanation of binning).

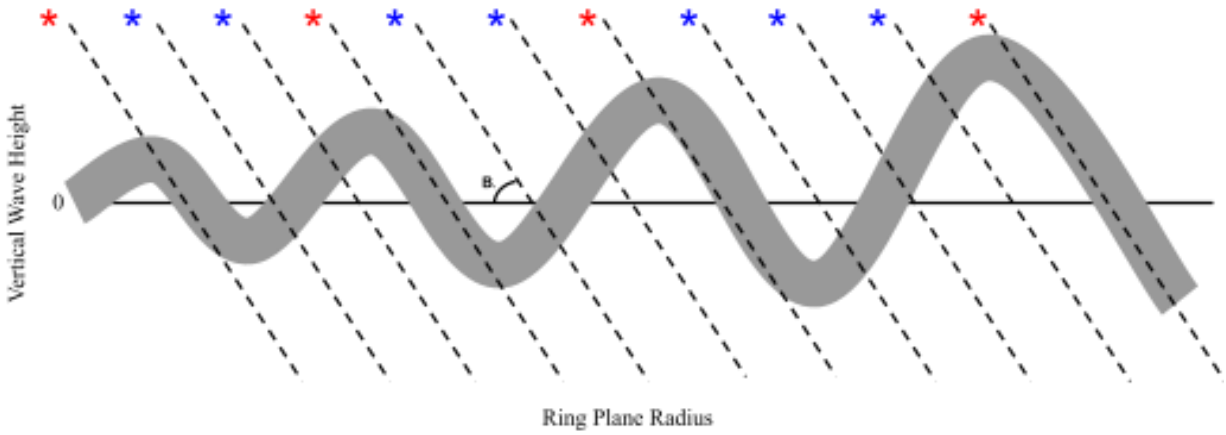

Figure 6. Illustration of Cassini stellar occultation incidence angle, B, of a bending wave (solid black line) compared to the horizontal ring plane. The vertical scale is greatly exaggerated. The dashed lines represent the line-of-sight between Cassini and the star at different points on the wave. Peaks in optical depth are marked by red asterisks, while troughs are marked with blue asterisks.

One way to visualize Saturn's rings is to analyze the optical depth of the region being studied (Fig. 7). Optical depth is a measure of the amount of light absorbed as it travels through a medium, with normal optical depth adjusting this value to simulate optical depth if measured perpendicular to the ring plane. The greater the overlap between the line-of-sight and the bending wave, the higher the observed optical depth (Fig. 6). Normal optical depth is calculated using the B angle in conjunction with the measured intensity of the star (I), the unobstructed intensity of the star (I_0), and any background signal present (b) using the following equation,

$$n = ln\ I0I\text{-}b \qquad \text{(Eq. 1)}$$

Highly absorbent, opaque regions having high optical depths and more transparent regions having low optical depths. Saturn's rings exhibit a wide range of optical depths and other features and can be grouped broadly into more optically dense rings (A, B, C) and less optically dense rings (D, E, G) (Fig. 8). The denser rings typically have optical depths greater than 0.1, while the less dense rings typically have optical depths below 10^{-3} (Colwell *et al.*, 2009). Density waves create a distinct pattern of alternating high and low optical depth that can be used to identify them.

Table 2 List of occultations

Occultation star (Rev)	Ingress (I) or Egress (E)	B	Radius (km)
α VIR (30)	I	17.3	151545-64010
α VIR (34)	I	17.3	153653-74536
α VIR (116)	I	17.3	144565-103057
α VIR (124)	E	17.3	70493-142430
α VIR (134)	I	17.3	143681-72604
α VIR (173)	E	17.3	109357-143407
α VIR (173)	I	17.3	143407-109357

Occultation star (Rev)	Ingress (I) or Egress (E)	B	Radius (km)
α VIR (210)	I	17.3	146048-70692
α VIR (211)	E	17.3	105299-125667
α VIR (211)	E	17.3	105299-125667
α VIR (211)	I	17.3	125667-105299
α VIR (232)	E	17.3	70190-143844
κ ORI (212)	I	5.2	148652-70932
κ ORI (279)	E	5.2	135211-167521
κ ORI (279)	I	5.2	167521-135211
κ ORI (280)	E	5.2	113448-150437
κ ORI (280)	I	5.2	150437-113448
κ ORI (281)	E	5.2	91253-153745
κ ORI (281)	I	5.2	153745-91253
β CEN (77)	I	66.7	144893-73333

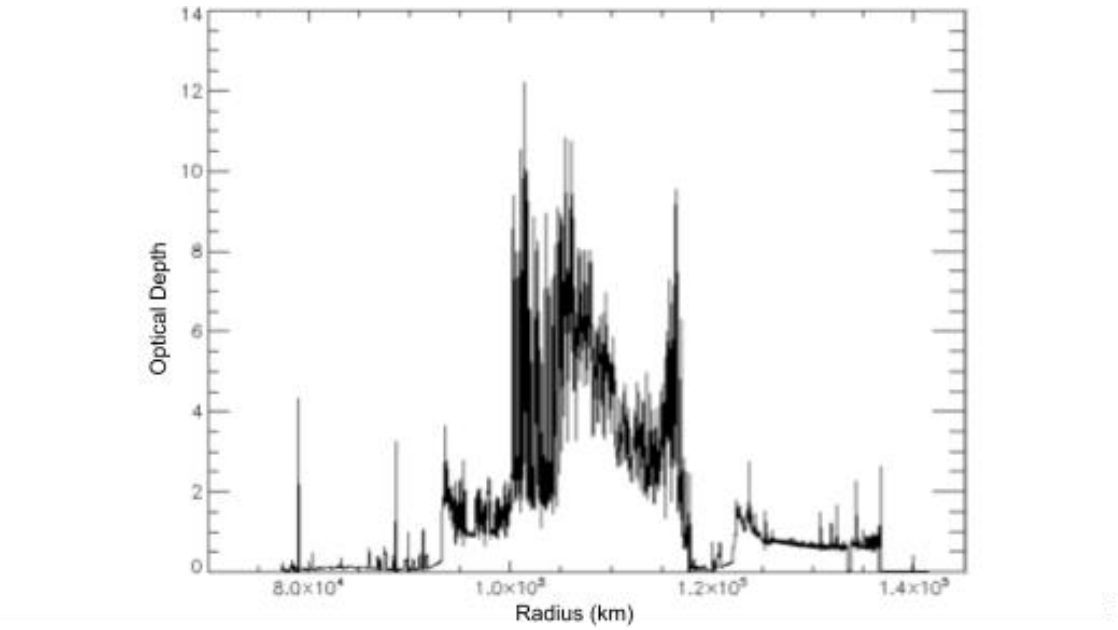

Figure 7. Optical depth profile of the rings from BetCen 077I.

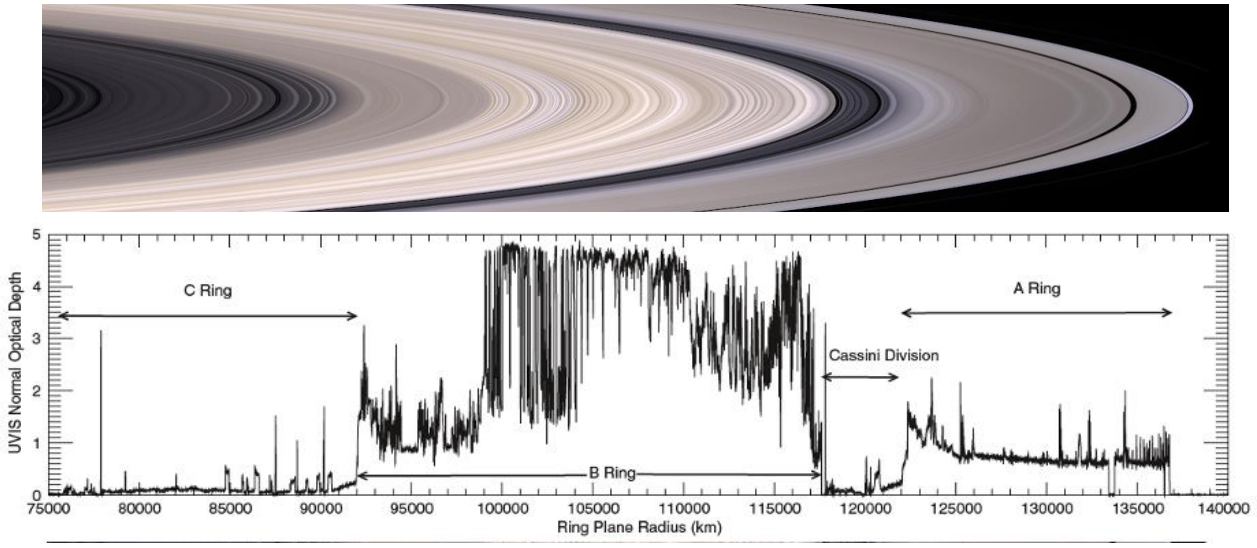

Figure 8. The top image shows the relative position of Saturn's rings and moons, and the bottom plot by Colwell et al. (2009) shows the optical depth profile of the C, B, and A rings as well as that of the Cassini division.

When plotting optical depth over ring plane radius, both density and bending waves will appear as repeating high-and-low optical depths. Figure 9 shows how, even in the unprocessed photon count data, the Mimas 5:3 DW is visible as periodic increases and decreases in intensity. When this data is converted to optical depth in Figure 10, we see the characteristic optical depth oscillation indicative of a wave.

Another method of plotting wave data is by using a wavelet transform. The wavelet transform involves separating the input signal in the frequency domain as well as identifying locations in the signal where a specific frequency is important, allowing for much clearer visualization of periodic signatures in data. Figures 11 and 12 illustrate this concept, with Figure 11 showing the optical depth profile of the Mimas 5:3 BW taken from AlpVir 116I and demonstrating the characteristic optical depth oscillation indicative of a wave. Figure 12 uses the same data but uses a weighted wavelet transform. When waves that adhere to the linear theory

are graphed in this way, the slope when plotting their wavenumber over the distance between Saturn's center is constant and the surface mass density can be assumed to be constant throughout the wave (Tiscareno *et al.*, 2007). As a wave travels further away from the resonance location, assuming the local surface mass density is constant, its wavelength will decrease and its wavenumber will increase. By comparing this ideal linear model with constant local surface mass density to the measured wave data, we can estimate the local surface mass density at a point a certain distance from the resonance and from Saturn. Lissauer (1985) used this relationship to derive equation (1), which relates the local surface mass density of the rings, σ, wavenumber of the wave, k, distance from the resonance location, d, and resonance location in units of Saturn's equatorial radius, R.

$$\sigma\ (g\ cm^{-2}) = \frac{0.325(m-1)2\pi}{R^4(\frac{\Delta k}{\Delta d})} \qquad \text{(Eq. 2)}$$

On a wavelet plot showing wavenumber over radial distance from Saturn, a periodic feature with unchanging wavelength will produce a horizontal signal, while a feature with a constantly changing wavenumber (and, therefore, wavelength) will also produce a linear signature but one which shows an upward (if the wavenumber is increasing) or downward (if the wavenumber is decreasing) slope. Bending waves will show an upward slope since they propagate towards Saturn.

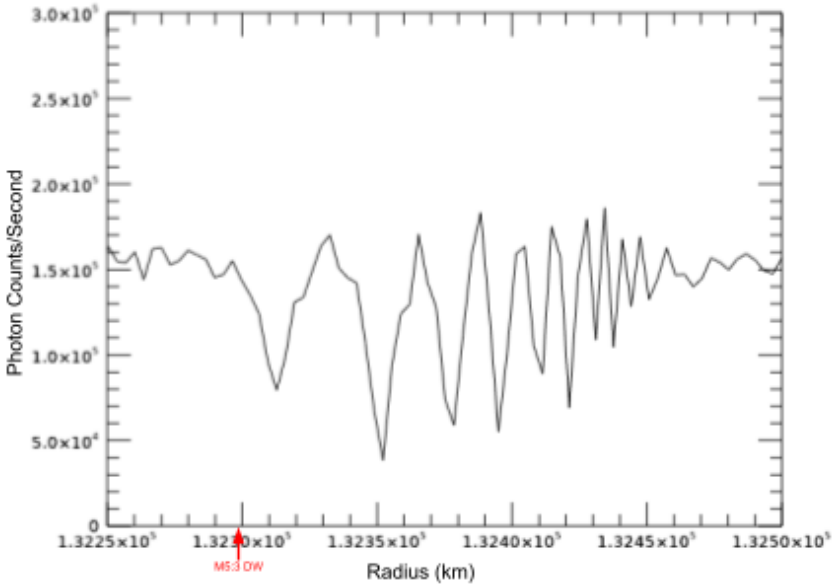

Figure 9. Raw data from BetCen 077I in the Mimas 5:3 DW region. Resonance location is marked in red.

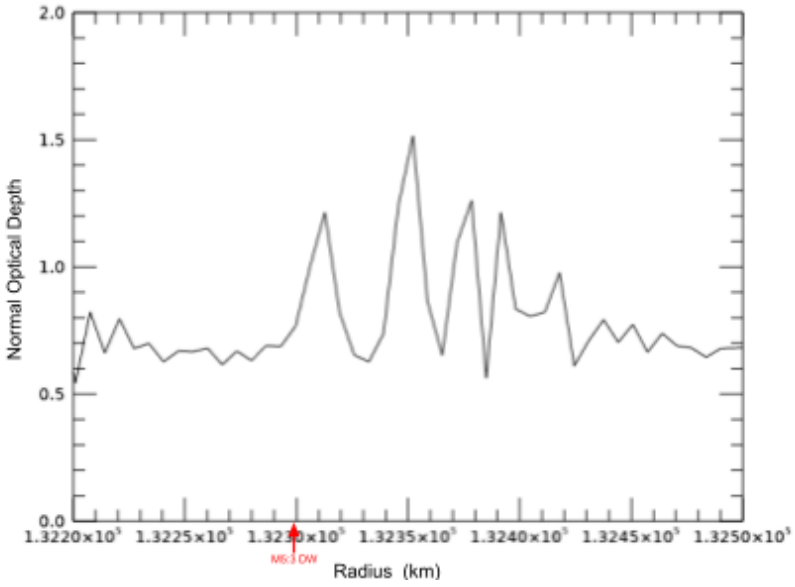

Figure 10. Optical depth profile of the Mimas 5:3 DW from BetCen 077I with resonance location marked in red.

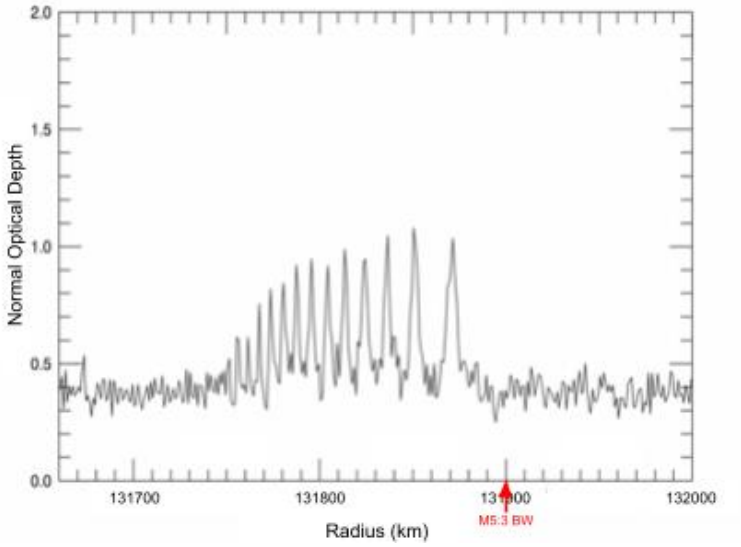

Figure 11. Optical depth profile of the Mimas 5:3 bending wave from AlpVir 116I, with the resonance location marked in red.

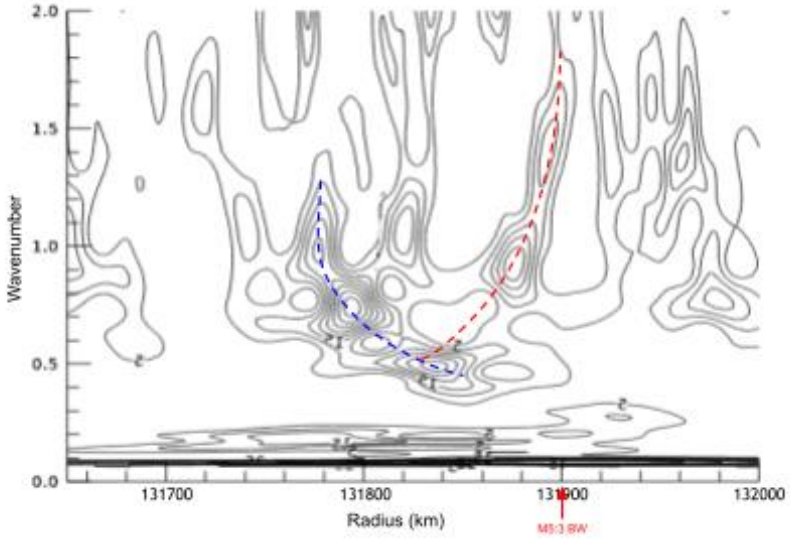

Figure 12. Weighted wavelet transform of the Mimas 5:3 BW from α Vir (dashed red line). The resonance location for the Mimas 5:3 BW is marked in red. The Prometheus 12:11 DW (dashed blue line) is also visible, propagating in the opposite direction.

4. METHODS

We used a weighted wavelet Z power transform to analyze various low B angle occultations in search of signals indicative of bending waves. Tiscareno *et al.* (2007) was the first to use the wavelet transform technique to process ring wave signals, demonstrating the power of this technique to identify and analyze waves that were previously unobserved due to their being closely packed together or having a low signal-to-noise ratio. Multiple occultations were co-added to increase the strength of the signal for weaker bending waves not easily identifiable within single occultations. The Fourier transform takes periodic data over time and converts it to amplitude over frequency by comparing the data to various circular paths of specific frequencies, amplitudes, and phase angles. By using several frequency filters, it is able to separate complex, mixed signals into their component parts for analysis. A windowed Fourier transform involves analyzing a succession of small segments from a time series, windowing them with a function of one's choice (a boxcar, a Gaussian window, etc) (Torrence and Compo, 1998). Due to this type of analysis requiring the use of a set scale for analysis, it is often necessary to analyze several window lengths in order to determine which is most appropriate. The drawback to this type of analysis is that the width of the piece of data analyzed has a large impact on the time and frequency resolutions, with narrower windows giving good time resolution but poor frequency resolution compared to wider windows and vise-versa.

A wavelet transform was chosen because a limitation of the Fourier transform is that it cannot be used for a signal whose frequency changes over time. The ability to do this is especially important when analyzing bending waves, due to the dominant frequency of the wave changing as it propagates inward (Tiscareno and Harris, 2018). This is known as a "chirp" function, which is a signal that increases or decreases with time, either linearly or exponentially.

For analyzing these types of signals, it is more appropriate to use a wavelet transform, such as the Morlet wavelet (Fig. 13) which is a sine wave multiplied by a Gaussian window (i.e. whose ends taper off to 0 in a bell curve shape) (Torrence and Compo, 1998). The Morlet wavelet, as a complex wave function, provides information about both the amplitude and the phase of the time series. Wavelet transforms enable us to analyze data whose frequency changes over time by comparing the wave data to the wavelet, with an adjustable width of the Gaussian Morlet wavelet.

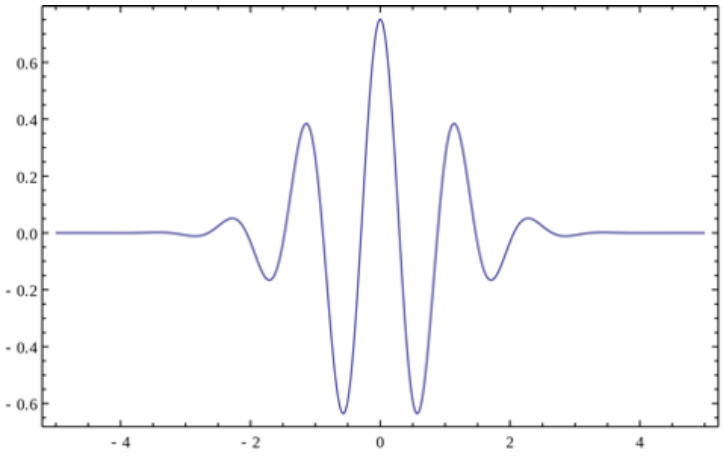

Figure 13. A Morlet wavelet

The choice of wavelet function may depend on various factors. The choice of orthogonal vs nonorthogonal wavelet analysis depends on whether the desired output is discrete “blocks" of wavelet power and a smaller, more closely-packed representation of the signal (orthogonal), or if wavelet amplitude is expected to fluctuate continuously and smoothly over a time series (nonorthogonal). A complex wave function will provide information about both the amplitude and phase of the data, whereas a real wavelet function will focus on the single component used to isolate the peaks. The width of a wavelet function determines the overall resolution, with a

narrow function giving good time resolution but poor frequency resolution, and a broad function giving the inverse. Finally, the shape of the chosen wavelet function should match the broad features of the time series, such as choosing a smooth function (a Morlet wavelet) for a time series with smooth variation. For the purposes of this research, the choice of wavelet function is not crucial as the different wavelet functions will give the same qualitative results when used to analyze wavelet power spectra (Torrence and Compo, 1998).

While individual occultations may not allow for clear visualization of wave structures, co-adding multiple wavelet transforms can help differentiate these weaker waves (Colwell et al., 2009). Co-adding wavelet data in this way increases confidence in the detection of periodic signatures by adding the power of persistent periodic signals present at specific wavelengths and radial locations found throughout multiple occultations (Hedman and Nicholson, 2016) while averaging out noise (Baille *et al*., 2011). This technique is especially useful when the region we are studying is optically dense or contains other features that make it difficult to distinguish wave signatures even with the power of the weighted wavelet transform. Figures 14 and 15 illustrate this concept, as they are both wave profiles of the Mimas 7:4 BW taken from occultations of KapOri. However, the data for Figure 14 only came from one occultation (KapOri 280E), while Figure 15 was plotted with the combined data of four occultations (KapOri 280E, 280I, 281E, and 281I). The bending wave is much more clearly visible in the combined plot, and the background noise has been greatly reduced. This power of this analysis technique is also demonstrated in the clear separation achieved between the Mimas 7:4 BW and the Prometheus 8:7 DW, which lie directly on top of one another and make their individual analysis difficult.

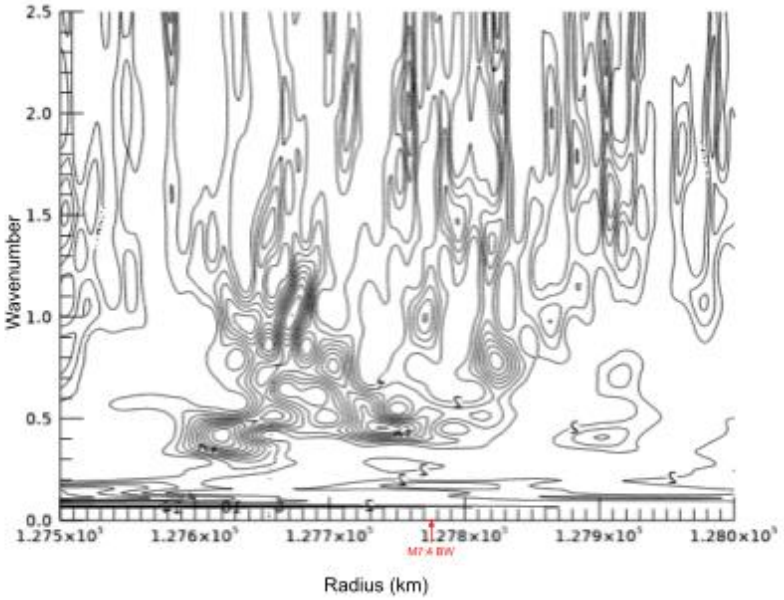

Figure 14. Weighted wavelet transform of the region surrounding the Mimas 7:4 BW using data from a single KapOri occultation. The resonance location of the Mimas 7:4 BW is marked in red.

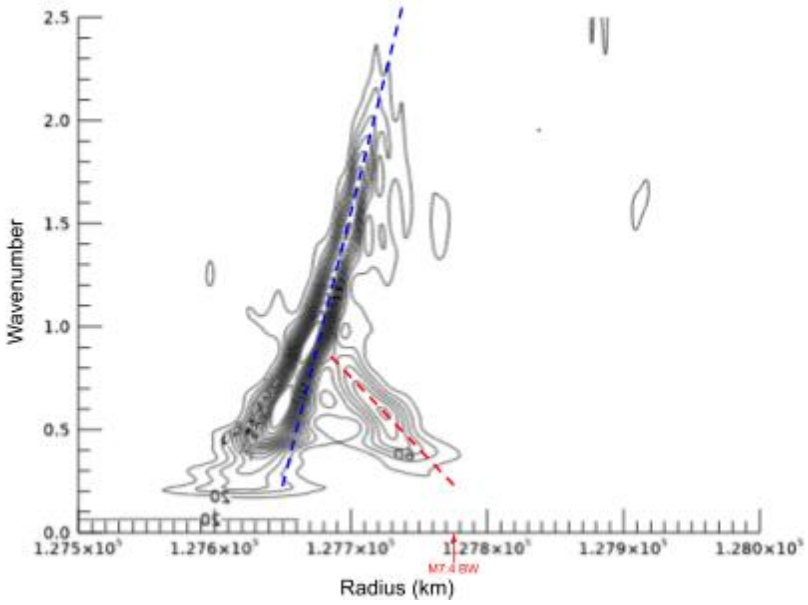

Figure 15. Wavelet transform of the Mimas 7:4 BW (red dashed line) using combined data from 4 KapOri occultations. The resonance location is marked in red. The Prometheus 8:7 DW is also distinctly visible on top of the Mimas 7:4 BW (blue dashed line)

4. RESULTS AND CONCLUSIONS

By utilizing the wavelet technique described above and co-adding the resulting wavelet profiles, we were able to visualize weaker bending waves in high optical density areas that would otherwise be hidden amongst the background signal or indistinguishable from the wavelet signature of stronger density waves at the same location. We were then able to use these combined plots to create two best-fit lines for the wave, one being the shallowest and one being the steepest slope we determined still fit the contours of the data. The resulting slopes were used to calculate the surface mass density range of the region using Equation 2. The line was fit to the linear portion of the wave further from the resonance location. For the Mimas 7:4 bending wave (Fig. 16), we calculated a σ range of 30 g cm^{-2} and 43 g cm^{-2}. This is within range of the value reported by Spilker *et al.* (2004) of 47 ± 6.2 g cm^{-2} thus supporting linear wave theory as it is currently understood. The Mimas 4:2 bending wave signature (Fig. 17) was created using 12 combined AlpVir occultations: 30E/I, 34E/I, 116I, 124E, 134I, 173 E/I, 210 I, 211 E, and 232 E. The surface mass density was estimated to be between 33 g cm^{-2} and 47 g cm^{-2}. Previously reported surface mass density values for this region, as cited in Colwell *et al.* (2009), are limited to 54 ± 10 g cm^{-2} and 70 ± 10 g cm^{-2}. Analysis of this wave is of particular interest due to the limited knowledge we have of the B ring due to it having very few observable density or bending compared to other ring regions (Colwell *et al.*, 2009).

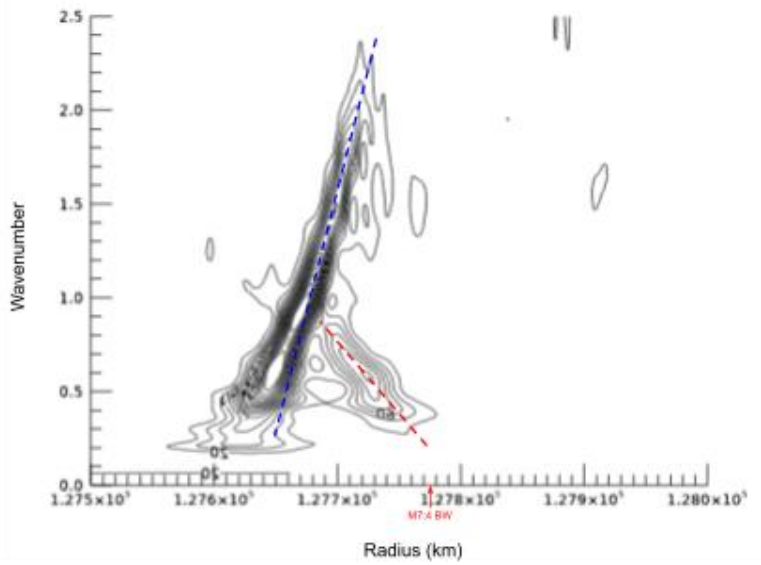

Figure 16. Wavelet profile of the Mimas 7:4 BW (red dashed line) from combined AlpVir and KapOri occultations, resonance location marked in red. The Prometheus 8:7 DW is also distinctly visible on top of the Mimas 7:4 BW (blue dashed line).

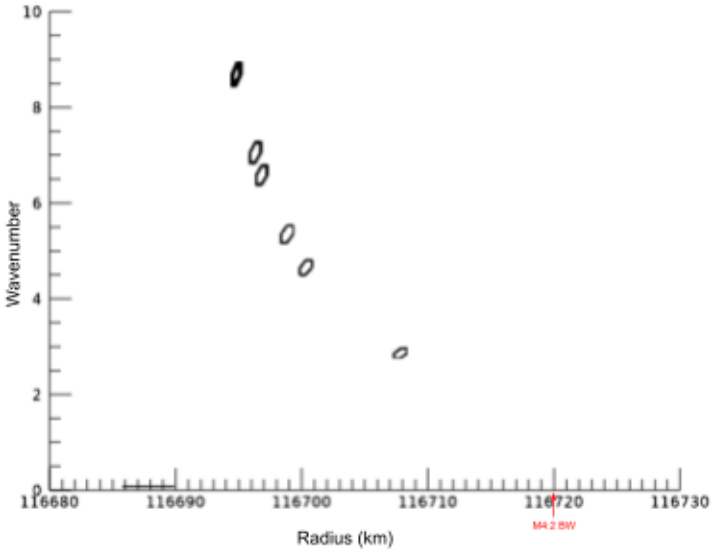

Figure 17. Wavelet profile of the Mimas 4:2 BW from 17 combined AlpVir occultations.

While analysis of the information from the Cassini mission has been extremely useful in furthering our understanding of the structure and dynamics of Saturn's rings, there are still many questions that remain about the underlying causes of the observed irregularities in the rings, as well as the nature of how they were formed. By combining the weighted wavelet transform with the process of co-adding wavelet signatures, these results lend further support to the continued use of these techniques to help study periodic features in less well-characterized regions of the rings. Future work could focus on exploration of the B- and C-rings, as well as look for evidence of other periodic signatures present within the rings not necessarily caused by perturbations from nearby moons.

REFERENCES

Baillie, K., Colwell, J.E., Lissauer, J. J., Esposito, L. W., Sremcevic, M., 2011. Waves in Cassini UVIS stellar occultations. Icarus 216, 292-308.

Colwell, J. E., Cooney, J. H., Esposito, L. W., Sremcevic, M., 2009. Density waves in Cassini UVIS stellar occultations. Icarus 200, 574-580.

Colwell, J. E., *et al.,* 2010. Cassini UVIS Stellar Occultation Observations of Saturn's Rings. The Astronomical Journal 140, 1569-1578.

Colwell, J. E., French, R. G., Marouf, E., Murray, C. D., Nicholson, P. D., Tiscareno, M. S., 2009. The Structure of Saturn's Rings. In Saturn from Cassini-Huygens. M. K. Dougherty, L. W. Esposito, T. Krimigis, Eds. (Springer Netherlands), pp. 375-412.

Cuzzi, J.N., Lissauer, J.J., Shu, F.H., 1981. Density waves in Saturn's rings. Nature 292, 703–707.

Cuzzi, J. N., *et al.*, 2002. Saturn's Rings: Pre-Cassini Status and Mission Goals. Space Science Reviews 104, 209-251.

Cuzzi, J. N., *et al.*, 2010. An Evolving View of Saturn's Dynamic Rings. Science 327, 1470-1475.

Esposito, L. W., 2009. Composition, structure, dynamics and evolution of Saturn's rings. Annual Review of Earth and Planetary Sciences 38, 383-410.

Esposito, L. W., Colwell, J. E., McClintock, W. E., 1998. Cassini UVIS observations of Saturn's rings. Planetary Space Science Volume 46, Number 9/10, 1221-1235.

Esposito, L. W., *et al.,* 2004. The Cassini Ultraviolet Imaging Spectrograph Investigation. Space Science Reviews 115, 299-361.

Gresh, D. L., Rosen, P. A., Tyler, G. L., 1986. An analysis of bending waves in Saturn's rings using Voyager radio occultation data. Icarus 68, 481-502.

Hedman, M. M., Nicholson, P. D., 2013. Kronoseismology using density waves in Saturn's C ring to probe the planet's interior. The Astronomical Journal 146, 12.

Hedman, M. M., Nicholson, P. D., 2014. More Kronoseismology with Saturn's rings. Monthly Notices of the Royal Astronomical Society Volume 444, Issue 2, 1369–1388.

Hedman, M. M., Nicholson, P. D., 2016. The B-ring's surface mass density from hidden density waves: less than meets the eye? Icarus 279, 109-124.

Lissauer, J. J., 1985. Bending waves and the structure of Saturn's rings. Icarus 62, 433-447.

Porco, C.C., West, R.A., Squyres, S., McEwen, A., Thomas, P., Murray, C.D., Delgenio, A., Ingersoll, A.P., Johnson, T.V., Neukum, G., Veverka, J., Dones, L., Brahic, A., Burns, J.A., Haemmerle, V., Knowles, B., Dawson, D., Roatsch, T., Beurle, K., Owen, W., 2004. Cassini imaging science: Instrument characteristics and anticipated scientific investigations at Saturn. Space Sci. Rev. 115, 363–497.

Porco, C.C., Baker, E., Barbara, J., Beurle, K., Brahic, A., Burns, J.A., Charnoz, S., Cooper, N., Dawson, D.D., Del Genio, A.D., Denk, T., Dones, L., Dyudina, U., Evans, M.W., Giese, B., Grazier, K., Helfenstein, P., Ingersoll, A.P., Jacobson, R.A., Johnson, T.V., McEwen, A., Murray, C.D., Neukum, G., Owen, W.M., Perry, J., Roatsch, T., Spitale, J., Squyres, S., Thomas, P., Tiscareno, M., Turtle, E., Vasavada, A.R., Veverka, J.,Wagner, R., West, R., 2005. Cassini imaging science: Initial results on Saturn's rings and small satellites. Science 307, 1226–1236.

Spilker, L. J., Pilorz, S., Lane, A. L., Nelson, R. M., Pollard, B., Russell, C.T., 2004. Saturn A ring surface mass densities from spiral density wave dispersion behavior. Icarus 171, 372–390.

Tiscareno, M. S., Burns, J. A., Nicholson, P. D., Hedman, M. M., Porco, C. C., 2007. Cassini imaging of Saturn's rings II. A wavelet technique for analysis of density waves and other radial structure in the rings. Icarus 189, 14–34.

Tiscareno, M. S., Harris, B. E., 2018. Mapping spiral waves and other radial features in Saturn's rings. Icarus 312, 157-171

Tiscareno, M. S., Hedman, M. M., Burns, J. A., Weiss, J. W., Porco, C. C., 2013. Probing the inner boundaries of Saturn's A ring with the Iapetus -1:0 nodal bending wave. Icarus 224, 201-208

Torrence, C., Compo, G. P., 1998. A practical guide to wavelet analysis. Bull. Am. Meteorol. Soc. 79, 61-78.